HHS Public Access

Author manuscript

IEEE Trans Biomed Eng. Author manuscript; available in PMC 2017 February 05.

Published in final edited form as:

IEEE Trans Biomed Eng. 2013 December ; 60(12): 3306–3313. doi:10.1109/TBME.2013.2280877.

Improved Sensing Pulses for Increased Human Head Depth Measurement Sensitivity With Electrical Impedance Spectroscopy

Giorgio Bonmassar [Senior Member, IEEE] and
AA Martinos Center, Harvard Medical School, Charlestown, MA 02129 USA

Michael H. Lev
Department of Radiology, Division of Neuroradiology, Massachusetts General Hospital, Harvard Medical School, Boston MA 02114 USA

Abstract

This paper describes an improved electrical impedance spectroscopy (EIS) stimulus paradigm, based on dual-energy pulses using the stochastic Gabor function (SGF) that may more sensitively assess deep brain tissue impedance than current single-pulse paradigms. The SGF is a uniformly distributed noise, modulated by a Gaussian envelope, with a wide-frequency spectrum representation regardless of the stimuli energy, and is least compact in the sample frequency phase plane. Numerical results obtained using a realistic human head model confirm that two sequential SGF pulses at different energies can improve EIS depth sensitivity when used in a dual-energy subtraction scheme. Specifically, although the two SGF pulses exhibit different tissue current distributions, they maintain the broadband sensing pulse characteristics needed to generate all the frequencies of interest. Moreover, finite-difference time domain simulations show that this dual-energy excitation scheme is capable of reducing the amplitude of weighted current densities surface directly underneath the electrodes by approximately 3 million times versus single stimulation pulses, while maintaining an acceptable tissue conductivity distribution at depth. This increased sensitivity for the detection of small, deep impedance changes might be of value in potential future EIS applications, such as the portable, point-of-care detection of deep brain hemorrhage or infarction.

Index Terms

Electrical impedance measurement; pulse generation; spectral analysis; stochastic systems

I. Introduction

IN this paper, we show that a new type of pulse excitation, the dual-energy pulse based on the stochastic Gabor function (SGF) [1], is optimal for electrical impedance spectroscopy

Correspondence to: Giorgio Bonmassar.

Color versions of one or more of the figures in this paper are available online at http://ieeexplore.ieee.org.

Authors' photographs and biographies not available at the time of publication.

(EIS) of deep brain parenchymal structures. Results from our group and others have shown that EIS has potential applications in point-of-care testing for rapid, affordable, and portable detection, assessment, and monitoring of patients with intracranial hemorrhage (ICH), stroke [2]–[5], and other forms of acute brain injury [6]–[8]. Cerebrospinal fluid (CSF) and *in situ* blood composed mainly of salt water and accounting for much of the brain's volume have baseline low resistance to current flow. The edema associated with acute (nonhemorrhagic) tissue injury, and the clot associated with acute ICH, cause complex—but distinguishable and localizable—frequency-dependent impedance changes, proportional to the size and composition of the intracranial lesion [9].

Currently, there is no portable, noninvasive monitoring device capable of detecting ischemic stroke, bleeding or rebleeding for ICH patients. Computed tomography (CT) and magnetic resonance imaging (MRI) are currently the first-line modalities for the diagnosis of acute brain injury—including both hemorrhagic and nonhemorrhagic lesions—but are limited in their battlefield and sport field availability. Moreover, even when portable CT scanners are available at forward unit hospitals, they remain a limited resource with undependable technical support and few contingency options for equipment breakdown, and cannot be deployed by corpsmen in the field for emergent triage of individuals with (otherwise unapparent) subdural and epidural hematomas.

Unfortunately, EIS is maximally sensitive to impedance changes at the electrode–skin interface [9], and is relatively insensitive to brain parenchymal changes due to the limited penetration of the probe current. Tissues in the human head are dispersive, and the EIS current density distribution depends on the sensing stimulation frequency. Tissues such as bone and CSF tend to divert currents entering the brain because their conductivities are very different compared to brain parenchyma. In order to measure the EIS signal, different approaches have been proposed. Because a sinusoidal sensing pulse at a single, individual frequency, however, might not fully characterize small differences in the dielectric constant between different tissues, alternative pulse generation schemes have been developed, mainly using multitone or frequency-sweep methods [9]. Indeed, our group is currently using a 0–50 kHz "white noise" stimulation pulse for preliminary human studies of patients with hemorrhagic and nonhemorrhagic stroke [7], [8], [10].

Because frequency difference imaging has the potential to further improve sensitivity for the detection of deep intracranial lesions, we propose an ideal probe current design based on the concept of dual energy. In CT scanning, dual energy is a relatively recent imaging technique that uses two different X-ray energies (typically 140 and 80 kV) in a single CT exposure. Bone or iodinated contrast material can be segmented based on their spectral properties, and can be subtracted to create an angiographic image [11].

In this paper, we describe—both in theory and with numerical examples—the design of a dual-energy pulse for EIS, specifically based on the SGF [12]. The SGF is a uniformly distributed noise modulated by a Gaussian envelope. Its behavior and propagation have been studied with an electromagnetic wave solver or finite-difference time domain (FDTD) [12]. The Gabor transform has also been proposed as a probe signal in impedance estimation for applications such as fault detection, due to the fact that it has an optimal localization

property in both the time and frequency domains [13]. The SGF was chosen as the basis for our dual-energy pulse stimulus because it reaps the benefits of a very wide-frequency bandwidth, while retaining a nonnarrow pulsed envelope in time.

The proposed method consists of probing using two sequential SGF pulses with two different principal energies (see Fig. 1). The Fourier transforms of each of the weighted SGF current stimulation pulses are subtracted, and the Fourier transforms of each of the weighted synchronous voltage responses are also subtracted. The resulting Fourier-transformed subtracted input and output values are then deconvolved to estimate the complex impedance as a function of frequency.

Our results show that the depth of penetration of two different SGF pulses, with two different principal energies, will vary in the lossy media [14] of the human head. Although these two different SGF pulses exhibit different tissue current distributions, they each maintain the broadband sensing pulse characteristics needed to stimulate all the frequencies of interest. In this paper, we present images of pulse penetration model using the SGF dual-energy subtraction scheme in a realistic human head simulation. By applying the weighted SGF dual-energy subtraction methodology, EIS sensitivity decreases relatively in regions that would otherwise receive the highest current density (e.g., skin, subcutaneous fat), but increases relatively in what would otherwise be low-current density regions, such as the brain parenchyma.

II. Theory

The SGF (see Fig. 2) is defined as [15]

$$\lambda_n = \xi_n g_n^{\sigma} \quad (1)$$

where $n \in [1 : N]$, ξ_n is a random Gaussian white noise process uniformly distributed in [−1; 1], and $g_n^s = \frac{exp[-\frac{n^2}{2s^2}]}{s\sqrt{2\pi}}$ is the Gaussian function. The ξ_n set is valid only if the resulting SGF is zero mean (i.e., $\langle \lambda_n \rangle = 0$). The power spectral density [16] of the SGF is

$$\wp_k = S_k^{\xi\xi} * \left| G_k^{1/s} \right|^2 \quad (2)$$

where $k \in [1 : N]$ is the frequency variable and $S_k^{\xi\xi}$ is the discrete Fourier transform, or FFT, of the autocorrelation function of the white noise process ξ_n; $G_k^{1/s}$ is the FFT of g_n^s. The whitening of the Gaussian in (1) flattens the frequency response. The short-time Fourier transform is used to determine the sinusoidal frequency and phase content of a signal inside a time window, following the spectral changes of the signal over time. The short-time Fourier transform of the SGF is

$$\Gamma_{k,m}=\sum_{n=1}^{N}\lambda_n w_{n-m}\, exp[-j2\pi nk] \quad (3)$$

where $m \in [1 : N]$ specifies the position of the time window and w_n is the time window function such that $\sum_{n=1}^{N}|w_n|^2=1$. By selecting a Gaussian, $w_n=g_n^s$, as the window function,

$$\Gamma_{k,m}=\sum_{n=1}^{N}\xi_n g_n^s \widehat{g_{n-m}^{s}}\, exp[-j2\pi nk] \quad (4)$$

and the short-time power spectral density becomes

$$\wp_{k,m}=S_k^{\xi\xi} * |G_k^{1/s} * G_k^{1/\widehat{s}}\, exp[j2\pi mk]\,|^2 \cong c g_m^{2\left(s+\widehat{s}\right)}. \quad (5)$$

The SGF has a Gaussian envelope in the time domain; its frequency representation (see Fig. 2, bottom) is very uniform. One of the main advantages of the Gabor functions is their time-frequency localization. This allows for the SGF excitation signal in broad bandwidth and fast impedance measurement. In this section, the SGF was studied in terms of localization in the time domain, which can be measured by estimating the time-frequency resolution to select the value for s, or pulse width of the SGF [15]. A more uniform sampling in frequency corresponds to a source excitation with lower concentration in the sample frequency phase plane [17]:

$$H\left(\Gamma_n\right)=\sum_{n=1}^{N}\|\Gamma_n\|^2\, log\, \left(\|\Gamma_n\|^2+\varepsilon\right) \quad (6)$$

where ε is an arbitrarily small constant introduced for regularization. Equation (7) has a form similar to the entropy function, $E(p_i) = -p_i \log(p_i)$; however, the resulting quantity is an estimate of frequency concentration when the Hermitian vector Γ_n is transformed into a real vector using the square norm.

The propagation of currents inside the human head can be expressed by the following set of quasi-static approximation [18]:

$$\begin{gathered}\nabla\left(\left(\sigma\left(\omega\right)+j\omega\varepsilon_0\varepsilon_r\left(\omega\right)\right)\right.\\ \left.\left(\mathbf{E}\left(\omega\right)+\mathbf{E_0}\left(\omega\right)\right)+\mathbf{J}_e\left(\omega\right)+\omega\boldsymbol{P}\left(\omega\right)\right)=0\end{gathered} \quad (7)$$

with the assumptions that the induced electric field is curl free, or equivalently that skin effect and wave propagation effects can be ignored. Assuming a time-harmonic electric

field, it is well known that in a lossy dispersive medium, the electric energy density in a point $P \in (x_0, y_0, z_0)$ in the medium [19] becomes

$$W_P(\omega) = \frac{1}{2}\sigma_P(\omega)\left|\boldsymbol{E}_P(\omega)\right|^2. \quad (8)$$

After discretizing and introducing the SGF with an external current applied along a direction **v** with power spectral densities $\boldsymbol{J}_{e,k} = \mathbf{v}\mathscr{P}_k$ in (6) discretized, the local conductivity is

$$\sigma_{P,k} = \frac{2W_{P,k}}{\left|\boldsymbol{E}_{P,k}\right|^2}. \quad (9)$$

When applying two SGF pulses at different times and subtracting the effect of the two different local energies $W^A_{P,k}, W^B_{P,k}$ and electric fields $\boldsymbol{E}^A_{P,k}, \boldsymbol{E}^B_{P,k}$:

$$\sigma_{P,k} = 2\left|\frac{W^A_{P,k}}{\left|\boldsymbol{E}^A_{P,k}\right|^2} - \frac{W^B_{P,k}}{\left|\boldsymbol{E}^B_{P,k}\right|^2}\right|. \quad (10)$$

$\sigma_{P,k}$ is not zero since the two SGF probing functions have different power spectral densities: $S^{\xi\xi}_k * \left|G^{1/s_1}_k\right|^2 \neq S^{\xi\xi}_k * \left|G^{1/s_2}_k\right|^2$, with different energies or variances (s_1^2 and s_2^2) and two different states of the white noise ergodic process (ξ_n).

III. Numerical Simulations

The geometry from a previously developed [20] 1 × 1 × 1 mm^3 resolution head model was adopted in the electromagnetic FDTD simulations with parameters presented in Table I. The overall simulated geometry dimensions were 170 mm in width, 217 mm in depth, and 238 mm in height. Each tissue of the head model was modeled under the common assumption of linearity of the $\vec{E}$-field, nondispersive, isotropic medium, and heterogeneous space using a one-pole Debye–Drude model based on its histological properties [21]. The Debye–Drude dispersion model was defined as follows [22]:

$$\hat{\varepsilon}_d(\omega) = \varepsilon_\infty + \frac{\Delta\varepsilon}{1 + j\omega\tau_1} + \frac{\sigma_1}{j\omega\varepsilon_0} \quad (11)$$

where σ_1 is the static ionic conductivity, ε_∞ is the permittivity at field frequencies $\omega\tau \gg 1$, ε_0 is the permittivity of free space, $\Delta\varepsilon = \varepsilon_s - \varepsilon_\infty$ is the magnitude of the dispersion, and ε_s is the permittivity at field frequencies $\omega\tau \ll 1$.

In the model, two standard EEG electrodes with 10-mm diameter were modeled with perfect electrical conductors (PEC) and were connected through PEC wires to a current source that generated the two SGF pulses: the lower energy SGF was defined with $s = 12.8$ and the higher energy with $s = 128$ both with $N_s = 10^5$. The weighted current density was defined as

$$\vec{J}_{w,k} = w\,\vec{J}_k^{A} - (1-w)\,\vec{J}_k^{B} \quad (12)$$

where $\vec{J}_k^{A}, \vec{J}_k^{B}$ are the current densities of the low- and high-energy SGF, respectively, with peak amplitude normalized to 1 A/m^2. All components are shown at 500 kHz, and were computed using the chirp transform (e.g., the "czt" command in MATLAB) of the electric fields and of the current densities distribution. All electrical components were computed using commercially available software (XFDTD v. 7, Remcom Inc., State College, PA) based on the FDTD algorithm [23], [24]. The geometrical grid consisted of 1-mm^3 uniform Yee cells [25]. The volume of the FDTD grid including the head model and the EIS electrodes was 4,642,730 Yee cells. The total size of the geometry, including the free space around the head model, was 323 × 373 × 323 mm^3. Seven perfectly matching layers were used for boundary conditions in all simulations [26]. The timestep used to ensure FDTD Courant–Friedrich–Levy stability was 1.92 ps [23]. The computation times for both SGF stimuli were 5 min for $N_s = 105$, respectively, using an eight-core Dell Precision T7500 desktop computer with 48 gigabyte of RAM on a C2070 graphics processing unit (Nvidia, Santa Clara, CA, USA) with 6-GB graphics memory.

IV. Results

FDTD simulations were performed to study the sensitivity or the current density of the proposed SGF dual-energy pulse in deep brain structures. Fig. 3 illustrates the distribution of the electric field magnitude $\left|\vec{E}\right|$ in the logarithmic scale (dB relative to 1 V/m) generated by the two different SGFs in a realistic head model [20] when used as a probe current pulse through the two EIS electrodes. The results are shown at 500 kHz in and around the head using two different values of the energy or variance s^2 for the SGFs (top and bottom). The higher energy SGF was defined with $s = 128$ and the lower energy with $s = 12.8$ both with $N_s = 10^5$. The higher energy SGF pulse had a $\left|\vec{E}\right|$ peak located in the occipital electrode of 580 V/m ($\angle 3.5\ 10^{-6}$ deg). The lower energy SGF pulse had a twofold decrease in the $\left|\vec{E}\right|$ peak of 207 V/m ($\angle 3.1\ 10^{-6}$ deg) also located in the occipital electrode. Both the higher and lower energy SGF pulses had null of $\left|\vec{E}\right|$ located in the central spinal canal.

Fig. 4 shows the estimated conductivity (dB relative to 1 Ω) of all the tissues in the head at 500 kHz, which was approximately the same when computed using all three pulsing schemes: higher, lower, and dual-energy SGF. Conductivity had an unbounded upper limit (i.e., Inf in MATLAB) in correspondence with the PEC material, where the electric field was null. Conductivity had null of σ located in the central spinal canal. The skin conductivity

was 0.4 S/m and white and gray matter σ was 0.1 S/m. Muscle had a conductivity of 2 S/m, cerebral spinal fluid 13 S/m, and bone 0.06 S/m.

The top of Fig. 5 shows how the profile of the weighted current density magnitude in (12) (center slice in dB relative to 1 A/m^2) as the weighting between the two SGF functions varies between $w = 0$ and $w = 1$. For the case $w = 1$ (high energy), the current density in the skin peaks, whereas for the case $w = 0$ (low energy), the current density in the center of the brain parenchyma peaks. The optimal weighting of $w = 0.2$ is shown at the bottom of Fig. 5, where at this value the amplitude of the current density on the skin is minimum compared to any other values of w.

In Fig. 6 are shown the estimated magnitudes of the current density for cases of 1) high energy (left), 2) low energy (right), and 3) when $w = 0.2$ (center, optimal value). In the case of $w = 0.2$, there is maximal sensitivity to CSF and blood compared to the cases of high or low energy alone. The current density in low-energy SGF peaked at 2.4 10^4 A/m^2 and high-energy SGF peaked at 4.7 10^3 A/m^2 located both in the occipital electrode. All current density magnitudes were null around the head model. Finally, the $w = 0.2$ case had a current density amplitude near the electrode of 3.1 10^{-6}A/m^2 or a reduction of approximately 3 million times compared to a single SGF stimulation pulse after normalization. The CSF is clearly the tissue that has the highest current density magnitude that peaks at 0.02 A/m^2.

V. Discussion

Using both the head model [20] and FDTD simulations [23], [24], we have shown that the proposed SGF dual-energy scheme results in improved sensitivity of EIS measurements of deep brain parenchymal impedance, compared to single stimulus methods, as the sensitivity is determined by the weighted current density [27].

This SGF dual-energy pulse scheme might provide a more accurate alternative to current “absolute frequency difference” and simple “linear frequency difference” EIS pulse stimulus paradigms, which subtract two single sinusoidal sensing pulses at two different individual frequencies to calculate impedance [28]. Unlike these frequency difference imaging methods, SGF dual-energy subtraction makes no assumptions regarding the shape of the impedance distribution as a function of frequency, i.e., in the dual-energy method, all subtractions are performed in frequency without requiring any interpolation.

The proposed dual-energy scheme might also be utilized to capture EIS measurements of events that occur in short time intervals, such as cardiac or respiratory monitoring applications. Given the properties of broadband and compactness, the SGF-based spectral impedance estimations are expected to be optimal for nonstationary measurements [12]. The use of broadband excitation also has precedent, and may provide faster and broader EIS estimation [9]. White noise EIS has been used to measure the dielectric properties of the cell membrane, and has achieved 1-ms measurements at 512 discrete frequencies, evenly distributed from 976.56 Hz to 500 kHz [29].

With regard to sampling strategies, sampling can be performed at the Nyquist rate. However, this method does not optimize the number of samples, which can be obtained by following

Landau's approach of signal demodulation followed by a lower sampling rate [30], where the demodulation is specifically implemented for the case of noise amplitude modulation [31]. An alternative sampling approach that does not require demodulation can be achieved by periodically nonuniform sampling [32], [33] that results in an optimal average sampling period equal to the SGF's bandwidth.

Energy, and hence power deposition, of our proposed multi-frequency method is larger than that of corresponding single- or dual-frequency methods, and is directly proportional to the excitation bandwidth, given that the SGF frequency spectrum is flat. Although heating of tissues is a theoretical possibility at very large bandwidths (and of course should be avoided as it may cause irreversible tissue damage), this is not a clinical concern at the lower, 0–50 kHz frequencies (and which are currently implemented using a continuous "white noise" stimulus in existing prototype EIS devices approved for clinical trials). As to whether very high SGF bandwidths (>1 MHz) might generate heating, the answer is clearly strongly dependent on the total power deposition and the current density (inversely proportional to electrode area) or the specific absorption rate of the multifrequency pulse [34]. Furthermore, the NRPB standard [35] limits the current density as follows: (0–10^0 Hz) 100 mA/m^2, (10^0–10^1 Hz) $100/f$ mA/m^2, (10^1–10^3 Hz) 10 mA/m^2, (10^3–10^7 Hz) $f/100$ mA/m^2, where f is the frequency in Hz. Therefore, Figs. 3 and 6 can be used to estimate the maximum $\left|\vec{E}\right|$ and $|\boldsymbol{J}|$ by adding +14 dB since the current density of the simulations @50 kHz was normalized to five times smaller than the NRPB limit (or adding +26 dB if following a recent and closely related Food and Drug Administration safety guidelines draft [36]).

The modeling of each tissue was carefully performed based on the very accurate morphometry of our head model and known tissue dielectric constants. Most tissues in the human head have complex but well-characterized anatomical features that were accurately reflected in our model (for example, cortical bone has a flat frequency response, but skull impedance varies due to other tissues present, such as fatty marrow) [37]. Despite this, there is clearly considerable intersubject variability in the shape and composition of head structures, which represents a limitation of our current model. It may be possible, however, to control these patient-specific variables in future models by incorporating concurrent CT or MRI morphometric measurements. Impedance imaging methods such as magnetic resonance electric properties tomography are also being developed [38] which could further help refine future models.

EIS has been used on a research basis for a wide variety of applications, such as measurement of osmotically induced cellular volume changes in a perfused rat model [39], and monitoring of intracellular resistance, membrane capacitance, and extracellular resistance [40]–[45].

Optimization of depth sensitivity in EIS measurement using the dual-energy SGF excitation pulses also has the potential to help develop proposed future point-of-care clinical applications, such as ICH and stroke detection [7], [8], [10], [46], [47] as well as noninvasive assessment of brain tumors [48], arteriovenous malformations, and radiation injury [49], cervical intraepithelial neoplasia [50], perinatal hypoxia [51] and asphyxia [52],

[53], thyroid nodules classification [54], and functional electrical stimulation efficacy [55], epilepsy [56], [57], and general brain function [58].

VI. Conclusion

We have shown that the use of an SGF dual-energy pulse generation paradigm can improve the sensitivity of EIS measurements of deep parenchymal tissues, compared to single stimulus methods. Indeed, simulations with FDTD have shown that the proposed SGF dual-energy excitation scheme is capable of reducing the amplitude of weighted current densities on the skin surface by approximately 3 million times compared to a single SGF stimulation pulse, while maintaining an acceptable tissue conductivity distribution in the brain parenchyma that could enhance the detection assessment of deep brain impedance values. This increased sensitivity for the detection of small, deep impedance changes might be of value in potential future EIS applications, such as the portable, point-of-care detection of deep brain hemorrhage or infarction [7], [8], [10].

Acknowledgments

The authors would like to thank Dr. M. Iacono for her help with running the FDTD simulations.

This work was supported in part by the National Institute of Biomedical Imaging and Bioengineering, National Institute of Health Subcontract through U of Cincinnati (5U54EB007954-04 sub award 005213) “Point-of-care” Center (POC-CENT) and in part by the Massachusetts General Hospital Clinical Research Center (1 UL1 RR025758-01) Harvard Clinical and Translational Science Center, from the National Center for Research Resources.

References

1. Bonmassar G, Iacono MI, Lev MH. Dual energy pulses for electrical impedance spectroscopy with the stochastic Gabor function. Conf Proc IEEE Eng Med Biol Soc. Aug.2012 2012:138–41. [PubMed: 23365851]
2. Horesh, L., Gilad, O., Romsauerova, A., Tizzard, A., Arridge, S., Holder, D. presented at the 6th Conf on Biomedical Applications of Electrical Impedance Tomography. University College London; London, UK: 2005. In stroke type detection by multi-frequency electrical impedance tomography MFEIT, Äîa feasibility study.
3. Clay MT, Ferree TC. Weighted regularization in electrical impedance tomography with applications to acute cerebral stroke. IEEE Trans Med Imag. Jun; 2002 21(6):629–37.
4. Yerworth RJ, Bayford RH, Brown B, Milnes P, Conway M, Holder DS. Electrical impedance tomography spectroscopy (EITS) for human head imaging. Physiol Meas. May.2003 24:477–89. [PubMed: 12812431]
5. Liu LX, Dong WW, Wang J, Wu Q, He W, Jia YJ. The role of noninvasive monitoring of cerebral electrical impedance in stroke. Acta Neurochir Suppl. 2005; 95:137–40. [PubMed: 16463838]
6. Liu XS, Stein EM, Zhou B, Zhang CA, Nickolas TL, Cohen A, Thomas V, McMahon DJ, Cosman F, Nieves J, Shane E, Guo XE. Individual trabecula segmentation (ITS)-based morphological analyses and micro finite element analysis of HR-pQCT images discriminate postmenopausal fragility fractures independent of DXA measurements. J Bone Miner Res. Feb.2012 27:263–272. [PubMed: 22072446]
7. Bonmassar, G., Iwaki, S., Schaechter, JD., Lev, MH., Belliveau, JW. presented at the 34th Annual Meeting Society for Neuroscience. San Diego, CA, USA: 2004. Abnormal distributions of spectral electrical impedance in response to a white noise current stimulus occur in chronic stroke patients.
8. Rosenthal E, Bonmassar G, Kamalian S, Borgie R, Schwamm L, Lev M. Electrical impedance spectroscopy (EIS) can non-invasively and portably detect subacute infarction and acute/subacute intracranial hemorrhage. presented at the Neurocritical Care Society 2012 Annual Meeting. 2012

9. Barsoukov, E., Macdonald, JR. Impedance Spectroscopy: Theory, Experiment, and Applications. 2nd. Hoboken, NJ, USA: Wiley-Interscience; 2005.
10. Bonmassar G, Iwaki S, Goldmakher G, Angelone LM, Belliveau JW, Lev MH. On the measurement of electrical impedance spectroscopy (EIS) of the human head. Int J Bioelectromagn. Jan 1.2010 12:32–46. [PubMed: 21152370]
11. Gambino O, Daidone E, Sciortino M, Pirrone R, Ardizzone E. Automatic skull stripping in MRI based on morphological filters and fuzzy c-means segmentation. Conf Proc IEEE Eng Med Biol Soc. Aug.2011 2011:5040–5043. [PubMed: 22255471]
12. Seo JK, Kim MO, Lee J, Choi N, Woo EJ, Kim HJ, Kwon OI, Kim DH. Error analysis of nonconstant admittivity for MR-based electric property imaging. IEEE Trans Med Imag. Feb; 2012 31(2):430–437.
13. Kawady TA, Ibrahim AE, Taalab AM. A Gabor transform-based universal fault detector for transmission lines. Proc 12th Int Middle-East Power Syst Conf. 2008:265–269.
14. Sommerfeld A. Über die Fortpflanzung des Lichtes in dispergierenden Medien. Ann Phys. 1914; 349:177–202.
15. Bonmassar G. The stochastic Gabor function enhances bandwidth in finite-difference-time domain S-parameter estimation. IEEE Trans Microw Theory Tech. Apr; 2007 55(4):601–606.
16. Kay S, Marple SJ. Spectrum analysis—A modern prospective. Proc IEEE. 1981; 69:1380–1419.
17. DeBrunner V, Ozaydýn M, Przebinda T. Resolution in time-frequency. IEEE Trans Signal Process. Mar; 1999 47(3):783–788.
18. Jackson, JD. Classical Electrodynamics. 3rd. Hoboken, NJ, USA: Wiley; 1998.
19. Webb KJ, Shivanand. Electromagnetic field energy in dispersive materials. J Opt Soc Am B. 2010; 27:1215–1220.
20. Makris N, Angelone L, Tulloch S, Sorg S, Kaiser J, Kennedy D, Bonmassar G. MRI-based anatomical model of the human head for specific absorption rate mapping. Med Biol Eng Comput. Dec.2008 46:1239–51. [PubMed: 18985401]
21. Gabriel C, Gabriel S, Corthout E. The dielectric properties of biological tissues: III. Parametric models for the dielectric spectrum of tissues. Phys Med Biol. 1996; 41:2271–2293. [PubMed: 8938026]
22. Luebbers R, Hunsberger FP, Kunz KS, Standler RB, Schneider M. A frequency-dependent finite-difference time-domain formulation for dispersive materials. IEEE Trans Electromagn Compat. Aug; 1990 32(3):222–227.
23. Kunz, KS., Luebbers, RJ. The Finite Difference Time Domain Method for Electromagnetics. Boca Raton, FL, USA: CRC Press; 1993.
24. Taflove, A., Hagness, SC. Computational Electrodynamics: The Finite-Difference Time-Domain Method. 2nd. Boston, MA, USA: Artech House; 2000.
25. Yee KS. Numerical solution of initial boundary value problems involving Maxwell's equations in isotropic media. IEEE Trans Antennas Propag. Mar; 1966 14(3):302–307.
26. Berenger JP. A perfectly matched layer for the absorption of electromagnetic waves. Comput Phys. 1994; 114:185–200.
27. Geselowitz DB. An application of electrocardiographic lead theory to impedance plethysmography. IEEE Trans Biomed Eng. Jan.1971 18:38–41. [PubMed: 5545046]
28. Packham B, Koo H, Romsauerova A, Ahn S, McEwan A, Jun SC, Holder DS. Comparison of frequency difference reconstruction algorithms for the detection of acute stroke using EIT in a realistic head-shaped tank. Physiol Meas. May.2012 33:767–86. [PubMed: 22531059]
29. Tao S, Shady G, Catia B, Nicolas GG, Hywel M. Broadband single cell impedance spectroscopy using maximum length sequences: theoretical analysis and practical considerations. Meas Sci Technol. Jul.2007 18:2859–2868.
30. Landau HJ. Sampling, data transmission, and the Nyquist rate. Proc IEEE. 1967; 55:1701–1706.
31. Journée HL, Manen J, Meer JJ. Demodulation of e.m.g.s. of pathological tremours. Development and testing of a demodulator for clinical use. Med Biol Eng Comput. Mar.1983 21:172–175. [PubMed: 6887991]

32. Yuan-Pei L, Vaidyanathan PP. Periodically nonuniform sampling of bandpass signals. IEEE Trans Circuits Syst— Part II: Analog Digital Signal Process. Mar; 1998 45(3):340–351.
33. Mishali M, Eldar YC. From theory to practice: Sub-Nyquist sampling of sparse wideband analog signals. IEEE J Sel Topics Signal Process. Apr; 2010 4(2):375–391.
34. Reilly, JP. Applied Bioelectricity: From Electrical Stimulation to Electropathology. New York, NY, USA: Springer-Verlag; 1998.
35. McKinlay A, Allen S, Dimbylow P, Muirhead C, Saunders R. NRPB. Restrictions on human exposure to static and time varying electromagnetic fields and radiation: Scientific basis and recommendations for the implementation of the Board's Statement. Doc NRPB. 1993; 4(5):7–63.
36. FDA. Draft guidance for industry and FDA staff: Class II special-controls guidance document: transcutaneous electrical nerve stimulator-with limited output for pain relief. 2010. [Online] Available: http://www.fda.gov/MedicalDevices/DeviceRegulationandGuidance/-GuidanceDocuments/ucm198585.htm
37. Tang C, You F, Cheng G, Gao D, Fu F, Dong X. Modeling the frequency dependence of the electrical properties of the live human skull. Physiol Meas. Dec.2009 30:1293–301. [PubMed: 19843982]
38. Xiaotong Z, Shanan Z, Bin H. Imaging electric properties of biological tissues by RF field mapping in MRI. IEEE Trans Med Imag. Feb; 2010 29(2):474–481.
39. Sasser DC, Gerth WA, Wu YC. Monitoring of segmental intra- and extracellular volume changes using electrical impedance spectroscopy. J Appl Physiol. May.1993 74:2180–7. [PubMed: 8335546]
40. Wang Q, Wang H, Cui Z, Yang C. Reconstruction of electrical impedance tomography (EIT) images based on the expectation maximum (EM) method. ISA Trans. Nov.2012 51:808–20. [PubMed: 22664353]
41. Dai T, Soleimani M, Adler A. EIT image reconstruction with four dimensional regularization. Med Biol Eng Comput. Sep.2008 46:889–99. [PubMed: 18633661]
42. Lionheart WR. EIT reconstruction algorithms: Pitfalls, challenges and recent developments. Physiol Meas. Feb.2004 25:125–42. [PubMed: 15005311]
43. Tang M, Wang W, Wheeler J, McCormick M, Dong X. The number of electrodes and basis functions in EIT image reconstruction. Physiol Meas. Feb.2002 23:129–40. [PubMed: 11876226]
44. Bayford RH, Boone KG, Hanquan Y, Holder DS. Improvement of the positional accuracy of EIT images of the head using a Lagrange multiplier reconstruction algorithm with diametric excitation. Physiol Meas. Nov; 1996 17(Suppl 4 A):49–57.
45. Kotre CJ. EIT image reconstruction using sensitivity weighted filtered backprojection. Physiol Meas. May; 1994 15(Suppl 2a):A125–A136. [PubMed: 8087034]
46. Atefi SR, Seoane F, Lindecrantz K. Electrical bioimpedance cerebral monitoring. Preliminary results from measurements on stroke patients. Proc 2012 Annu Int Conf IEEE Eng Med Biol Soc. 2012:126–129.
47. Liu L, Dong W, Ji X, Chen L, He W, Jia J. A new method of noninvasive brain-edema monitoring in stroke: cerebral electrical impedance measurement. Neurol Res. Jan.2006 28:31–7. [PubMed: 16464360]
48. Romsauerova A, McEwan A, Horesh L, Yerworth R, Bayford RH, Holder DS. Multi-frequency electrical impedance tomography (EIT) of the adult human head: initial findings in brain tumours, arteriovenous malformations and chronic stroke, development of an analysis method and calibration. Physiol Meas. May.2006 27:S147–S161. [PubMed: 16636407]
49. Kun S, Ristic B, Peura RA, Dunn RM. Algorithm for tissue ischemia estimation based on electrical impedance spectroscopy. IEEE Trans Biomed Eng. Dec.2003 50:1352–1359. [PubMed: 14656064]
50. Tidy J, Brown B, Healey T, Daayana S, Martin M, Prendiville W, Kitchener H. Accuracy of detection of high-grade cervical intraepithelial neoplasia using electrical impedance spectroscopy with colposcopy. BJOG. Jan 4.2013 120:400–410. [PubMed: 23289897]
51. Seoane F, Lindecrantz K, Olsson T, Kjellmer I, Flisberg A, Bagenholm R. Spectroscopy study of the dynamics of the transencephalic electrical impedance in the perinatal brain during hypoxia. Physiol Meas. Oct.2005 26:849–863. [PubMed: 16088073]

52. Lingwood BE, Healy GN, Kecskes Z, Dunster KR, Gray PH, Ward LC, Colditz PB. Prediction of outcome following hypoxia/ischaemia in the human infant using cerebral impedance. Clin Neurophysiol. Feb.2009 120:225–230. [PubMed: 19121601]

53. Seoane F, Ward LC, Lindecrantz K, Lingwood BE. Automated criterion-based analysis for Cole parameters assessment from cerebral neonatal electrical bioimpedance spectroscopy measurements. Physiol Meas. Aug.2012 33:1363–1377. [PubMed: 22828035]

54. Zheng B, Tublin ME, Klym AH, Gur D. Classification of thyroid nodules using a resonance-frequency based electrical impedance spectroscopy: A preliminary assessment. Thyroid. Dec 23.2012 23:854–862.

55. Wilks SJ, Richner TJ, Brodnick SK, Kipke DR, Williams JC, Otto KJ. Voltage biasing, cyclic voltammetry, & electrical impedance spectroscopy for neural interfaces. J Vis Exp. 2012

56. Holder D. Electrical impedance tomography of brain function: Its potential advantages for imaging epileptic activity. Proc IEE Colloq Electr Eng Epilepsy: Successful Partnership (Ref No 1998/444). 1998:7/1–7/5.

57. Fabrizi L, Sparkes M, Horesh L, Perez-Juste Abascal JF, McEwan A, Bayford RH, Elwes R, Binnie CD, Holder DS. Factors limiting the application of electrical impedance tomography for identification of regional conductivity changes using scalp electrodes during epileptic seizures in humans. Physiol Meas. May.2006 27:S163–S174. [PubMed: 16636408]

58. Holder DS. Electrical impedance tomography (EIT) of brain function. Brain Topogr. 1992; 5:87–93. [PubMed: 1489654]

59. Li QX, Gandhi OP. Thermal implications of the new relaxed IEEE RF safety standard for head exposures to cellular telephones at 835 and 1900 MHz. IEEE Trans Microw Theory Tech. 2006; 54(7):3146–3154.

60. Collins CM, Liu W, Wang J, Gruetter R, Vaughan JT, Ugurbil K, Smith MB. Temperature and SAR calculations for a human head within volume and surface coils at 64 and 300 MHz. J Magn Reson Imag. May.2004 19:650–6.

61. DeMarco SC, Lazzi G, Wentai L, Weiland JD, Humayun MS. Computed SAR and thermal elevation in a 0.25-mm 2-D model of the human eye and head in response to an implanted retinal stimulator—Part I: Models and methods. IEEE Trans Antennas Propag. 2003; 51(9):2274–2285.

62. Gabriel, C., Gabriel, S. Compilation of the dielectric properties of body tissues at RF and microwave frequencies. 1996. [Online]. Available: http://niremf.ifac.cnr.it/docs/DIELECTRIC/Report.html

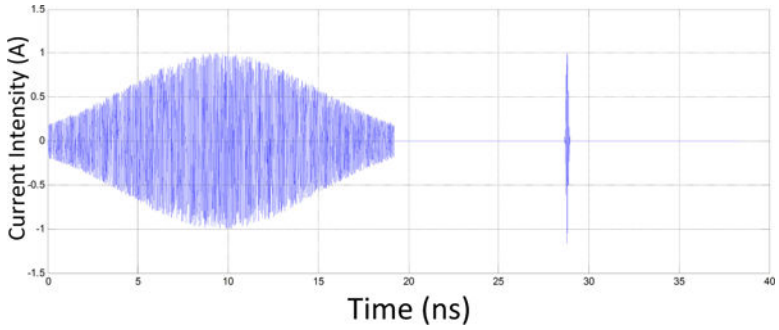

Fig. 1.

Dual-energy SGF pulses used in the FDTD simulations. A delay of 19.2 ns separates the high-energy pulse ($s = 128$) and the following low-energy SGF ($s = 12.8$).

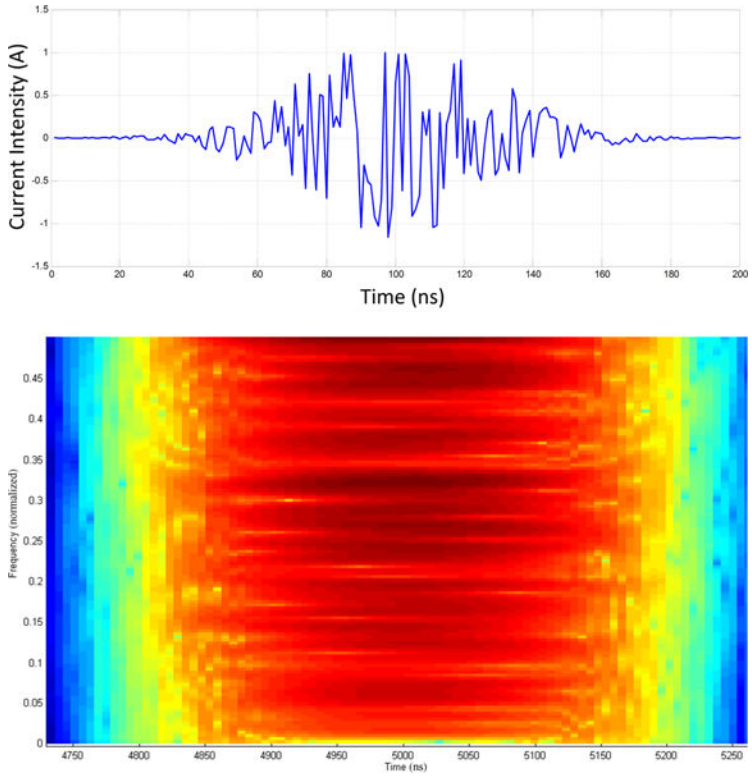

Fig. 2.

Low-energy pulse (s = 12.8) SGF in time (see top and Fig. 1) and its spectrogram (bottom) [12].

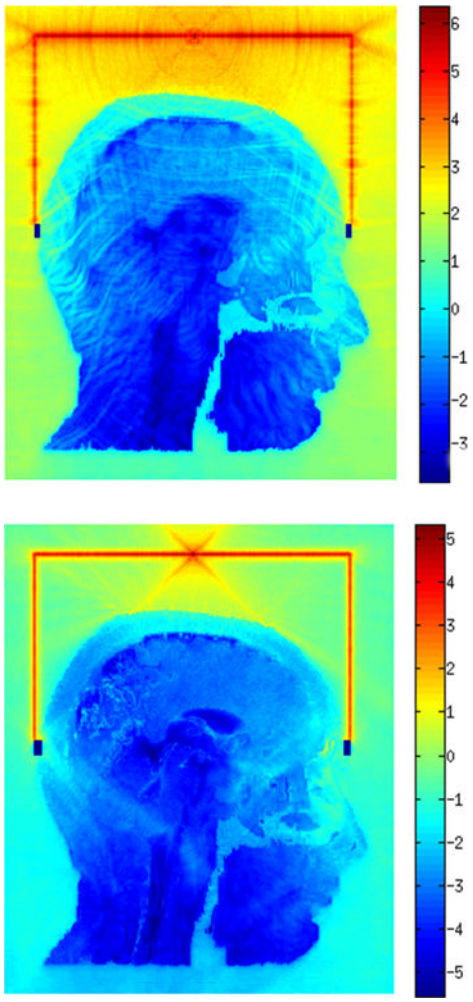

Fig. 3.

FDTD estimate of $\left|\vec{E}\right|$ at 500 kHz in a logarithmic scale (dB relative to 1 V/m) in the midline sagittal head model simulation, with: (top) SGF (s = 128) and (bottom) SGF (s = 12.8).

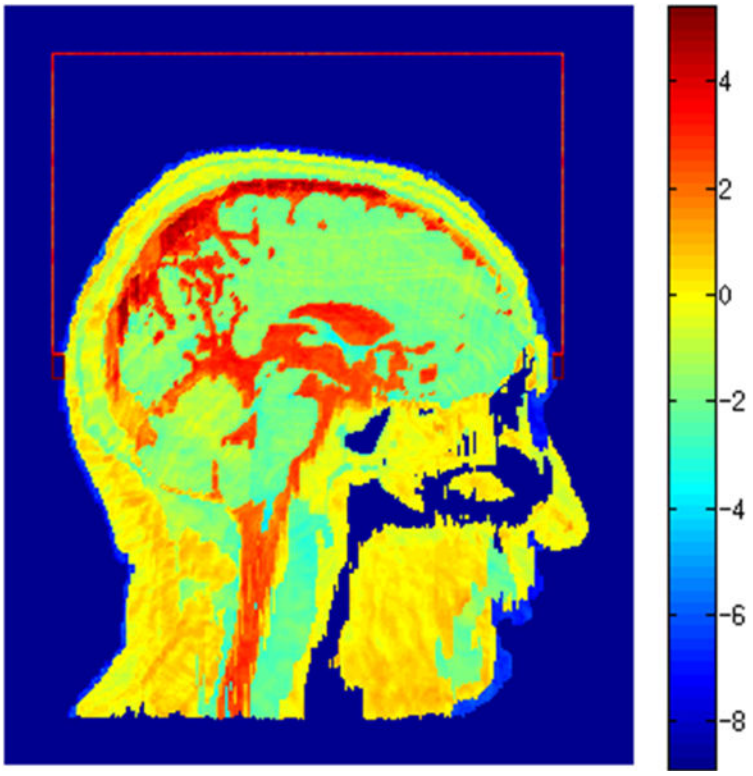

Fig. 4.

FDTD estimate at 500 kHz of conductivities in the log scale (dB relative to 1 Ω) for all stimuli, in the midline sagittal head model.

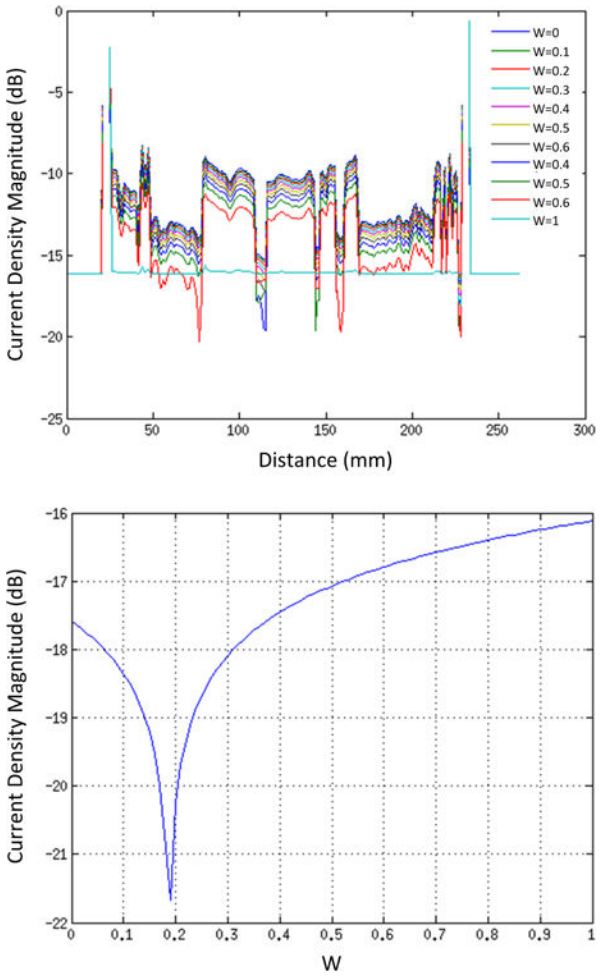

Fig. 5.

Current density magnitude (dB relative to 1 A/m^2) changes as a function of posterior-to-anterior distance along the midline at the level of the body of the corpus callosum in the head model simulation shown in Fig. 6 (top, with color coded *w*-values). The current density magnitude is minimized at a *w*-value of approximately 0.2 (bottom) in the model, which corresponds to a minimal current density on the skin surface.

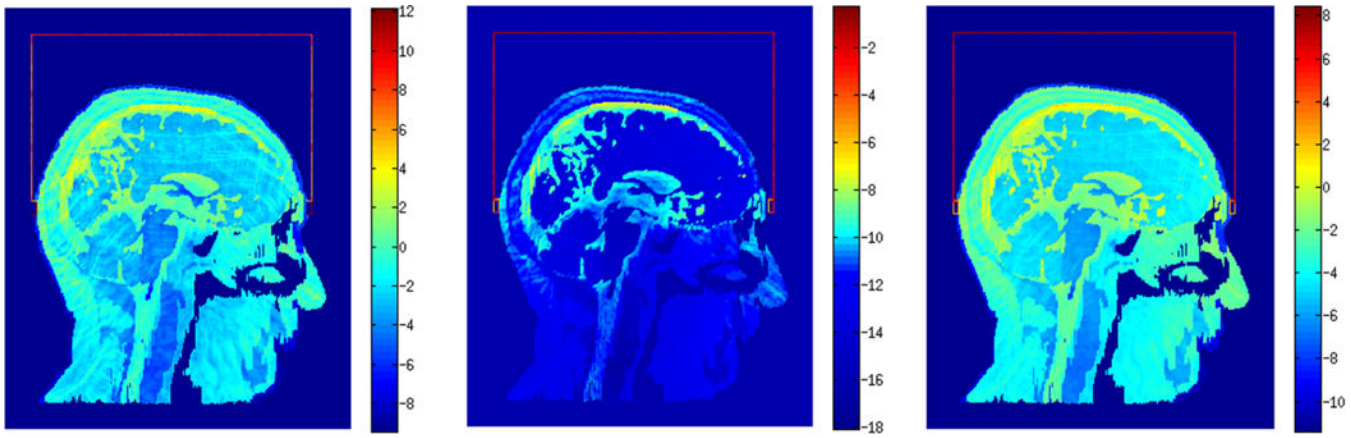

Fig. 6.

FDTD estimate at 500 kHz of the amplitude of the current densities (dB relative to 1 A/m^2 at the sagittal midline head, for $s = 128$ (left), $s = 12.8$ (right), and weighted (dual energy) with $w = 0.2$ (center).

TABLE I

List of Segmented Head Anatomical Structural Entities and Their Physical Properties Including Densities and Electrical Properties as Proposed in [21] or if Labeled:

	σ_0 (S/m)	ε^∞	$\Delta\varepsilon$	τ (ms)
3rd Ventricle	2	4	0.00E+00	15.915
4th Ventricle	2	4	0.00E+00	15.915
Adipose[a]	0.035	2.5	1.00E+07	15.915
Air (Resp./Diges./Sinus)[b]	0	1	0.00E+00	1
Aqueous Humor([a,c])	1.5	4	0.00E+00	15.915
Bone (Facial)[b]	0.02	2.5	1.00E+05	15.915
Brain Stem[a]	0.02	4	4.50E+07	5.305
Cavum vergi	2	4	0.00E+00	15.915
Cerebro Spinal Fluid	2	4	0.00E+00	15.915
Connective Tissue	0.128	3.5	2.50E+07	11.368
Cornea[c]	0.4	4	0.00E+00	15.915
CSF_Subarachnoid[a]	2	4	0.00E+00	15.915
Diploe[b]	0.07	2.5	2.00E+07	15.915
Dura[a]	0.5	4	1.00E+06	15.915
Ear/Pinna[a]	0.15	4	4.00E+07	15.915
Epidermis/Dermis[a]	0	4	0.00E+00	15.915
Inner Table[b]	0.02	2.5	1.00E+05	15.915
L/R Accumbens area	0.02	4	4.50E+07	5.305
L/R Amygdala	0.02	4	4.50E+07	5.305
L/R Amygdala Anterior	0.02	4	4.50E+07	5.305
L/R Caudate	0.02	4	4.50E+07	5.305
L/R Cerebellum Cortex	0.04	4	4.50E+07	5.305
L/R Cerebellum White Matter[a]	0.04	4	4.50E+07	5.305
L/R Cerebral Cortex[a]	0.02	4	4.50E+07	5.305

	σ_0 (S/m)	ε^∞	$\Delta\varepsilon$	τ (ms)
L/R Cerebral White Matter	0.02	4	4.50E+07	7.958
L/R Hippocampus	0.02	4	4.50E+07	5.305
L/R Inferior Lateral Ventricle[(a)]	2	4	0.00E+00	15.915
L/R Lateral Ventricle	2	4	0.00E+00	15.915
L/R Putamen	0.02	4	4.50E+07	5.305
L/R Thalamus Proper	0.02	4	4.50E+07	5.305
L/R Ventral DC	0.02	4	4.50E+07	5.305
L/RPallidum	0.02	4	4.50E+07	5.305
Lens[(c)]	0.3	4	4.00E+07	15.915
Mastoid/Air Cells	0	1	0.00E+00	1
Muscle[(d)]	0.2	4	2.50E+07	2.274
Nasal-Structures	0.15	4	4.00E+07	15.915
Nerve[(a)]	0.0006	4	4.00E+07	15.915
Optic Chiasm[(a)]	0.02	4	4.50E+07	7.958
Orbital Fat	0.035	2.5	1.00E+07	15.915
Outer Table[(b)]	0.02	2.5	1.00E+05	15.915
Retina/Choroid/Sclera[(a)]	0.5	4	5.00E+07	15.915
SC-Fat/Muscle	0.105	3.25	1.75E+07	5.116
Soft Tissue	0.128	3.5	2.50E+07	11.368
Spinal Cord	0.0006	4	4.00E+07	15.915
Subcutaneous Tissue	0.128	3.5	2.50E+07	11.368
Teeth	0.02	2.5	1.00E+05	15.915
Tongue	0.25	4	4.00E+07	15.915
Vitreous Humor	1.5	4	0.00E+00	15.915

(a)[59];

(b)[60];

(c)[61]

(d)[62]